A variational model for the hyperfine resolved spectrum of VO in its ground electronic state

Qianwei Qu, Sergey Yurchenko and Jonathan Tennyson
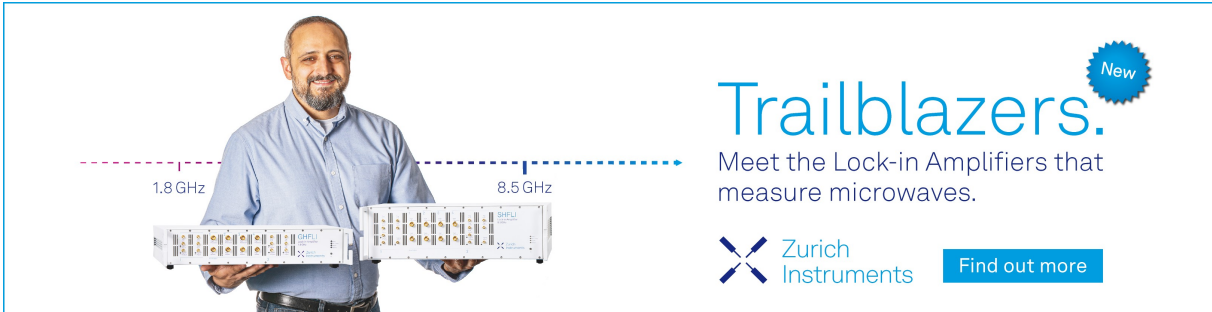
A variational model for the hyperfine resolved spectrum of VO in its ground electronic state

Qianwei Qu, Sergei N. Yurchenko and Jonathan Tennyson[1, a)]

Department of Physics and Astronomy, University College London,

London WC1E 6BT, United Kingdom

(Dated: 26 August 2022)

A variational model for the infra-red spectrum of VO is presented which aims to accurately predict the hyperfine structure within the VO $X\,^4\Sigma^-$ electronic ground state. To give the correct electron spin splitting of the $X\,^4\Sigma^-$ state, electron spin dipolar interaction within the ground state and the spin-orbit coupling between $X\,^4\Sigma^-$ and two excited states, $A\,^4\Pi$ and $1\,^2\Sigma^+$, are calculated *ab initio* alongside hyperfine interaction terms. Four hyperfine coupling terms are explicitly considered: Fermi-contact interaction, electron spin-nuclear spin dipolar interaction, nuclear spin-rotation interaction and nuclear electric quadrupole interaction. These terms are included as part of a full variational solution of the nuclear-motion Schrödinger equation performed using program Duo, which is used to generate both hyperfine-resolved energy levels and spectra. To improve the accuracy of the model, *ab initio* curves are subject to small shifts. The energy levels generated by this model show good agreement with the recently derived empirical term values. This and other comparisons validate both our model and the recently developed hyperfine modules in Duo.

---

a)j.tennyson@ucl.ac.uk

I.   INTRODUCTION

Vanadium monoxide (VO) is an open shell diatomic molecule which absorbs strongly in the near infrared and visible region of the spectrum. These absorptions are of importance for astrophysics where VO is known to be an important component of the atmosphere of cool stars.[1] Recently attention has turned to the possible role of VO in the atmospheres of exoplanets where it has been suggested that alongside TiO, VO absorption can change the temperature profile of the planet's atmosphere.[2] Some tentative detections of VO in exoplanet atmospheres have been reported[3–8] but none of these can be regarded as secure. There are two reasons for this. First, the spectra of VO and TiO are heavily overlapped making them very hard to disentangle at low resolution. Secondly, while the availability of a high-resolution TiO line list suitable for high-resolution spectroscopic studies[9] has led to the confirmation of TiO in exoplanetary atmospheres,[10–12] the corresponding VO line list[13] is not of sufficient accuracy to be used in similar studies.[14] Both the TiO and VO line lists cited were produced using similar methodology by the ExoMol project[15] but a major difference between them is due to the underlying atomic physics. While ^{16}O and ^{40}Ti both have nuclear spin, I, equal to zero, the dominant isotope of vanadium, ^{51}V, has $I = 7/2$. The interaction between the spin of unpaired electrons and the nuclear spin yields a very pronounced hyperfine structure which manifests itself at even moderate resolution. This hyperfine structure reduces parts of the ^{51}V^{16}O spectra to "blurred chaos at Doppler-limited resolution"[16]. Progress in identifying VO in exoplanetary atmospheres using high resolution spectroscopy requires the development of a model which includes a treatment of these hyperfine effects. These effects were not considered in the ExoMol VOMYT line list.[13]

A full survey of available high resolution spectroscopic data for VO has recently been completed by Bowesman *et al.*[17] as part of a MARVEL (measured active rotation vibration energy levels) study of the system. The nuclear hyperfine structure of ^{51}V^{16}O has been measured[18–22] and modeled by effective Hamiltonians.[22,23] However, for the the X $^4\Sigma^-$ ground electronic state, the experiments only gave the hyperfine constants for the lowest ($v = 0$) vibrational level and therefore provide limited information for the observations of hot VO spectra involving higher vibrational levels.

Hyperfine structure in molecular spectra are usually treated using perturbation-theory based effective Hamiltonians; these are usually accurate enough to reconstruct the energy

levels using the assumption that hyperfine effects arise from small perturbations. Thus, effective Hamiltonians are widely used for fitting measured hyperfine-resolved energies or transitions, see Refs.22 and 23 for examples involving VO. However, the VOMYT line list[13] shows that interactions between the electronic states reshape the line positions and intensities of VO. Although we focus on the $X\,^4\Sigma^-$ electronic ground state of VO in this paper, the spin-orbit couplings between the low-lying $X\,^4\Sigma^-$ and $1\,^2\Sigma^+$ states as well as the $X\,^4\Sigma^-$ and $A\,^4\Pi$ states are also included in our model with the aim of obtaining the correct spin splittings for the $X\,^4\Sigma^-$ state. This allows us to construct a full, predictive spectroscopic model of the ground state which can be used as input to the variational, diatomic spectroscopic program DUO[24] which we have recently extended to give a full variational treatment of hyperfine effects.[25] This paper presents the development of this model.

II.   COMPUTATIONAL DETAILS

The electronic structure of VO has been investigated in numerous works.[26–36] Among them, the results for excited states represented by multi-reference configuration interaction (MRCI) wavefunctions are more accurate.[33–36] The most recent one by McKemmish *et al.*[35] laid the basis of the ExoMol VO linelist, VOMYT.[13] We also perform MRCI level calculations in this work to get the potential and spin-orbit coupling curves for the electronic states of interest. The electron spin-dipolar interaction and hyperfine coupling curves of $X\,^4\Sigma^-$ were obtained at the complete active space self consistent field (CASSCF) level.

A.   Quartet states

In this work, the potential energy and spin-orbit coupling curves are calculated using MOLPRO 2015[37] at the MRCI level. The energies are also improved by adding a Davidson correction (+Q).

First, the ground $X\,^4\Sigma^-$ state was calculated on its own to avoid effects from other electronic states. The active space used is larger than employed by McKemmish *et al.*,[35] as the work of Miliordos *et al.*[33] shows that the occupation of 4p orbitals of vanadium is not negligible. In this work, the 1s orbital of oxygen and the 1s, 2s, 2p, 3s, 3p orbitals of vanadium were treated as doubly occupied. The active space includes the 2s, 2p orbitals of

oxygen and 4s, 3d, 4p orbitals of vanadium. In the four irreducible representations of C_{2v} group, *viz.* a_1, b_1, b_2, a_1, the numbers of occupied orbitals are $(12, 5, 5, 1)$ while the default setup was used to specify the closed, core orbitals as $(6, 2, 2, 0)$. We used the the internally contracted MRCI algorithm (icMRCI) implemented in MOLPRO. The basis set used in our calculation is aug-cc-pVnZ $n = 3, 4, 5$[38,39] so that we can estimate the potential energy curve at the complete basis set (CBS) limit by extrapolation.

According to Miliordos *et al.*,[33] ionic avoided crossings are expected around 2.75 Å, while we found a discontinuity in the dipole moment around 1.9 Å. We tried to add a second $^4\Sigma^-$ state but failed to find an avoided crossing structure in that region.

Off-diagonal spin-orbit interaction between the X$\,^4\Sigma^-$ and A$\,^4\Pi$ states contributes to the spin splitting of X$\,^4\Sigma^-$. As A$'\,^4\Phi$ and A$\,^4\Pi$ have the same irreducible representations in the C_{2v} group, it is impossible to omit the A$'\,^4\Phi$ in MRCI calculations. Therefore, we calculated the A$\,^4\Pi$ and A$'\,^4\Phi$ states together with the X$\,^4\Sigma^-$ states using the same active space but only with the aug-cc-pVQZ basis set.

B.   Interaction of doublet states with X$\,^4\Sigma^-$

Previous studies[13,35] show that the spin splitting of the X$\,^4\Sigma^-$ state of VO is dominated by the off-diagonal spin-orbit interaction between its X$\,^4\Sigma^-$ and $1\,^2\Sigma^+$ states.

The $1\,^2\Sigma^+$ state of VO, designated a$\,^2\Sigma^+$ in the experimental work of Adam *et al.*,[40] is easily obtained in a CASSCF calculation with MOLPRO when its `LQUANT` (*i.e.* the projection of orbit angular momentum on the internuclear axis) is assigned. However, a MOLPRO MRCI calculation may converge to the $1\,^2\Gamma$ state, which has degenerate A$_1$ and A$_2$ representations. The $1\,^2\Delta$ state also has the same irreducible representations and is lower than $1\,^2\Sigma^+$. In principle, the three states $1\,^2\Sigma^+$, $1\,^2\Gamma$ and $1\,^2\Delta$ should be optimized simultaneously in the ^{2}A$_1$ symmetry block. Our calculation therefore included these three low-lying doublets states of VO together with its ground state. The two higher $^2\Pi$ states were also included in the work of McKemmish *et al.*[35] but are not considered here.

We must provide a reasonable CASSCF reference for the MRCI calculations. The $1\,^2\Sigma^+$ and $1\,^2\Gamma$ states have the same electron configuration as and X$\,^4\Sigma^-$ while $1\,^2\Delta$ has a different one.[41] Thus, we initially calculated only the $1\,^2\Delta$ and ground state, and then subsequently added one $^2\Gamma$ state and one $^2\Sigma^+$ state. Nonetheless, we could not obtain the correct $1\,^2\Delta$

state in a state-average CASSCF calculation including $^4\Sigma^-$, $^2\Gamma$, $^2\Delta$ and $^2\Sigma^+$ when the closed orbitals were set to $(6, 2, 2, 0)$. To make the reference wavefunctions physically appropriate, we closed more orbitals, $(8, 2, 2, 0)$, in CASSCF calculation, while we still used the closed $(6, 2, 2, 0)$ space in the subsequent icMRCI calculation. Again we used an aug-cc-pVQZ basis set.

C.   Electron spin dipolar coupling and nuclear hyperfine coupling curves

The electron spin-spin coupling was treated as an empirical fine tuning factor by McK-emmish *et al.*.[13] Using the quantum chemistry program ORCA,[42] we calculated the electron spin-spin dipolar contribution to the zero-field splitting $\boldsymbol{D}$ tensor of the ground state at the CASSCF level with eleven electrons distributed in ten active orbitals.

Fully-resolved hyperfine splittings have been observed in the $v = 0$ vibrational levels of the X $^4\Sigma^-$ state. We calculated the nuclear hyperfine $\boldsymbol{A}$ tensor and the nuclear electric quadrupole coupling constant in ORCA,[42] with the aim of predicting the hyperfine structure in vibrationally-excited levels of VO.

The zero field splitting tensor was calculated with an aug-cc-pVTZ basis set. The nuclear magnetic $\boldsymbol{A}$-tensor and electric quadrupole coupling constant were calculated with an aug-cc-pwCVQZ basis set.

The nuclear spin-rotation coupling constants were calculated with another quantum chemistry program, DALTON[43] 2020.0, at the CASSCF level with an aug-cc-pVQZ basis set. The active space is the same as used in ORCA.

We failed to find a quantum chemistry program which calculates the electron spin-rotation constant γ and therefore used the constant empirical value determined for $v = 0$ instead (See Table IV).
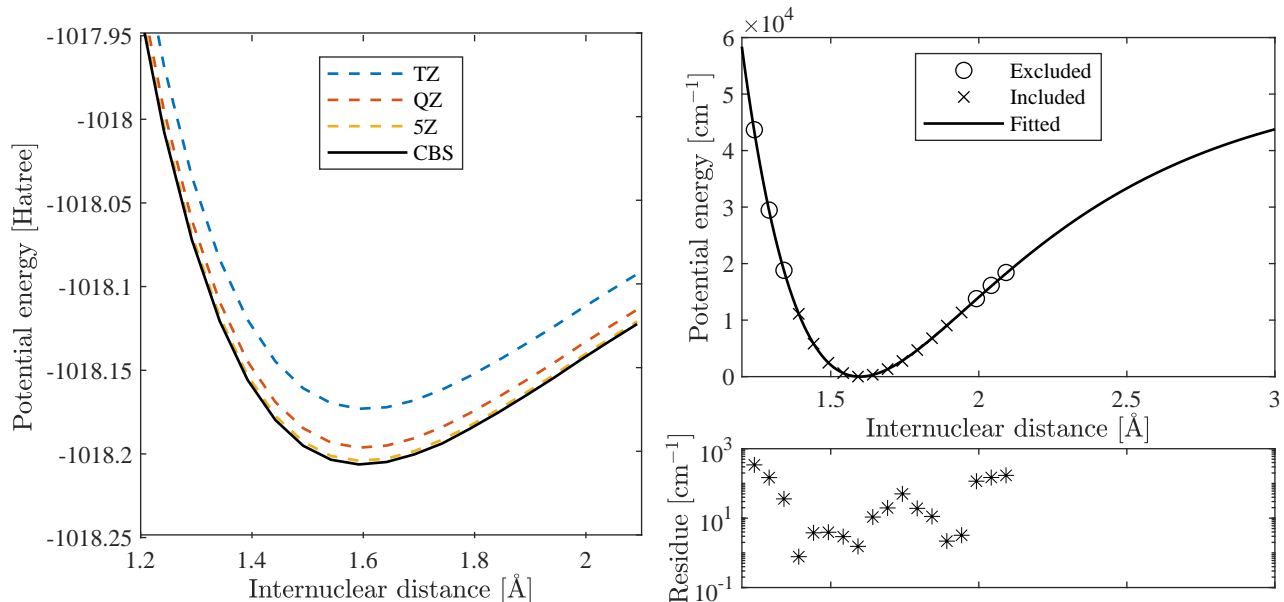
FIG. 1.   The lefthand panel shows the MRCI+Q potential energy curves of the $X\,^4\Sigma^-$ state calculated with aug-cc-pVnZ basis sets and the estimated one at complete basis set limit. The extrapolated potential energy curve is fitted with a second-order extended Morse oscillator (EMO) function. The right-bottom panel shows the fitting residues.

III.   AB INITIO RESULTS

A. $X\,^4\Sigma^-$ potential energy curve

The dashed curves in Fig. 1 are the *ab initio* potentials of the $X\,^4\Sigma^-$ state of VO. We estimated its potential energies at the CBS limit using the formula

$$E(n) = E_{\mathrm{CBS}} + \alpha \exp(-\beta n)$$

and obtained the solid potential energy curve shown in the left panel of Fig. 1.

The *ab initio* curves were calculated to build the spectroscopic model of VO. For numerical stability purposes, we fitted the discrete points with continuous curves. The extrapolated potential energy curve at the CBS limit was fitted to a second-order extended Morse oscillator (EMO) function:[24]

$$V(r) = T_{\mathrm{e}} + (A_{\mathrm{e}} - T_{\mathrm{e}})\left[1 - \exp\left(-\beta_{\mathrm{EMO}}(R)\,(R - R_{\mathrm{e}})\right)\right]^2, \tag{1}$$

where R and R_e is the internuclear distance and its value at the equilibrium point and A_{e} is the asympotic energy relative to the minimum of the ground electronics state. β_{EMO} is

6

expressed as

$$\beta_{\text{EMO}}(R) = b_0 + b_1\, y(R) + b_2\, y^2(R), \tag{2}$$

where $y(R)$ is given by:

$$y(R) = \frac{R^4 - R_{\text{e}}^4}{R^4 + R_{\text{e}}^4}. \tag{3}$$

Only the points given as crosses in the righthand panel of Fig. 1 were included in the fit to give a better approximation of the lower vibrational levels. Although the calculated potential energies marked by circle were excluded, they are still well represented by the fitted curve. The EMO parameters are listed in Table I.

The fitted PEC is not sensitive to the extrapolation formula in the region of interest (*i.e.* $E \leq 10\,000\,\text{cm}^{-1}$). Figure 2 compares the fitted EMO PECs of two extrapolation formulae: $E'(n) = E_{\text{CBS}} + \alpha/(n+1/2)^4$ and $E(n) = E_{\text{CBS}} + \alpha \exp(-\beta n)$. The EMO parameters corresponding to $E'(n)$ are listed in Table I too.

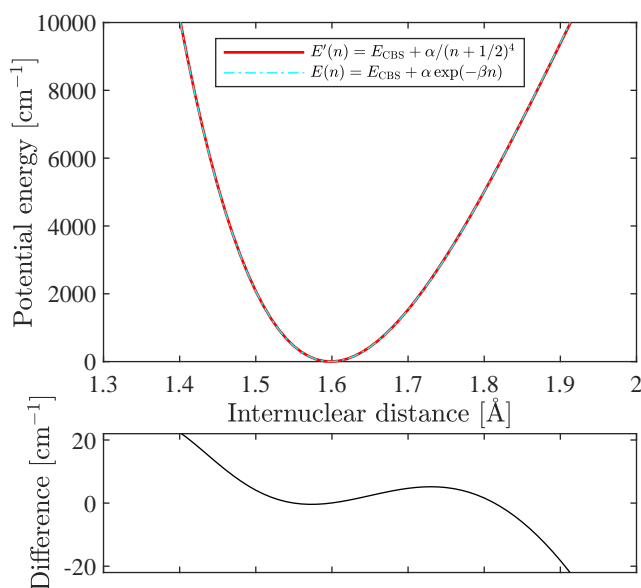FIG. 2.   Fitted PECs corresponding to two different extrapolation formulae as shown in the legend. The bottom panels show the energy difference between the two curve.

B.   Potentials of $A\,^4\Pi$ and $1\,^2\Sigma^+$

The calculated potential energy curves for the quartet and doublet states are shown in Fig. 3. The energies are shifted such that the corresponding $X\,^4\Sigma^-$ ground state of each set

TABLE I. Optimized EMO parameters of the $X\,^4\Sigma^-$ state.

Parameter	$E(n) = E_{\text{CBS}} + \frac{\alpha}{(n+1/2)^4}$	$E'(n) = E_{\text{CBS}} + \alpha e^{-\beta n}$
T_e [cm^{-1}]	0	0
R_e [cm]	1.598 438 63	1.598 355 33
D_e [cm^{-1}]	52790	52790
b_0 [Å^{-1}]	1.837 543 49	1.840 427 24
b_1 [Å^{-1}]	$-9.626\,810\,17 \times 10^{-3}$	$-1.623\,770\,24 \times 10^{-2}$
b_2 [Å^{-1}]	$-1.484\,134\,84 \times 10^{-1}$	$-1.802\,404\,76 \times 10^{-1}$

has the same energy zero. The potentials of $A\,^4\Pi$ and $1\,^2\Sigma^+$ were fitted with second-order EMO functions whose parameters are listed in Table II.
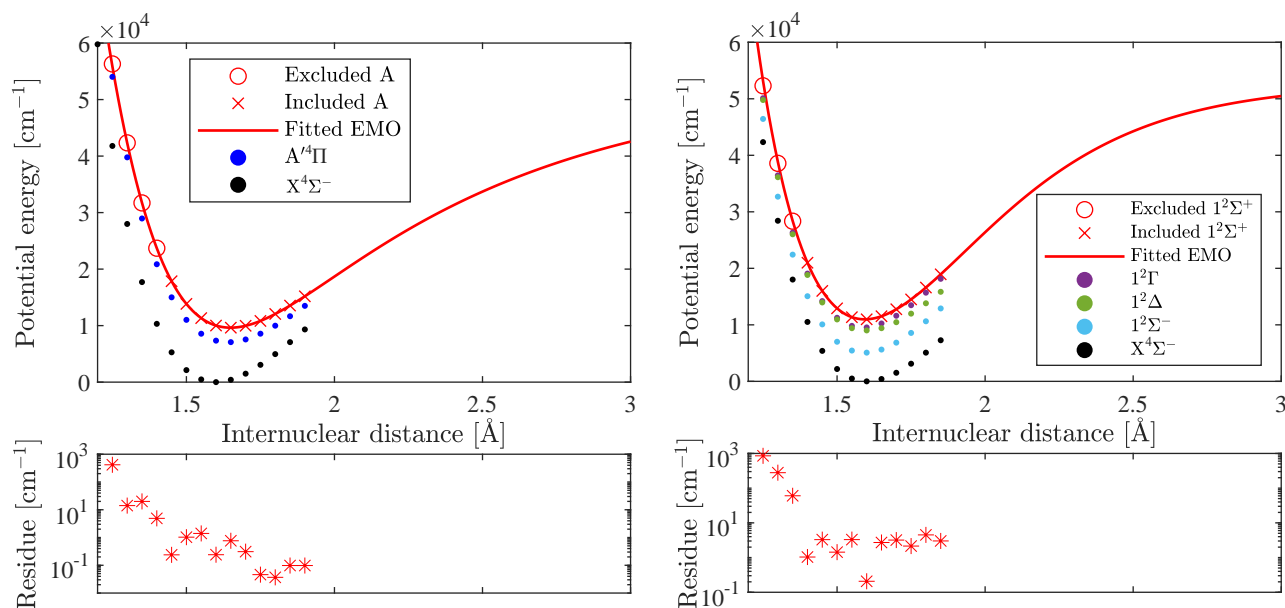
FIG. 3. Calculated potential energy curves of the quartet states (left) and doublet states (right) of VO. The curves of $A\,^4\Pi$ and $1\,^2\Sigma^+$ were fitted with EMO functions. The bottom panels show the fitting residues.

C. Spin-orbit couplings

The calculated spin-orbit coupling curves are shown in the left panel of Fig. 4. Note that the spin-orbit coupling constant has a phase of i as MOLPRO uses a Cartesian representa-

TABLE II. Optimized EMO parameters of the excited states.

Parameter	A $^4\Pi$	$1\,^2\Sigma^+$
T_e [cm^{-1}]	$9.634\,452\,79 \times 10^3$	$1.097\,399\,04 \times 10^4$
R_e [cm]	$1.649\,119\,57$	$1.593\,447\,21$
D_e [cm^{-1}]	52790	52790
b_0 [Å^{-1}]	$1.818\,147\,51$	$2.126\,803\,13$
b_1 [Å^{-1}]	$-8.353\,850\,40 \times 10^{-2}$	$3.162\,274\,70 \times 10^{-1}$
b_2 [Å^{-1}]	$-3.145\,101\,29 \times 10^{-1}$	$1.982\,856\,41 \times 10^{-1}$

tion. The figure demonstrates the real curves multiplied an extra constant $-\mathrm{i}$, which were fitted with polynomials

$$p(R) = \sum_i a_i\, R^i. \tag{4}$$

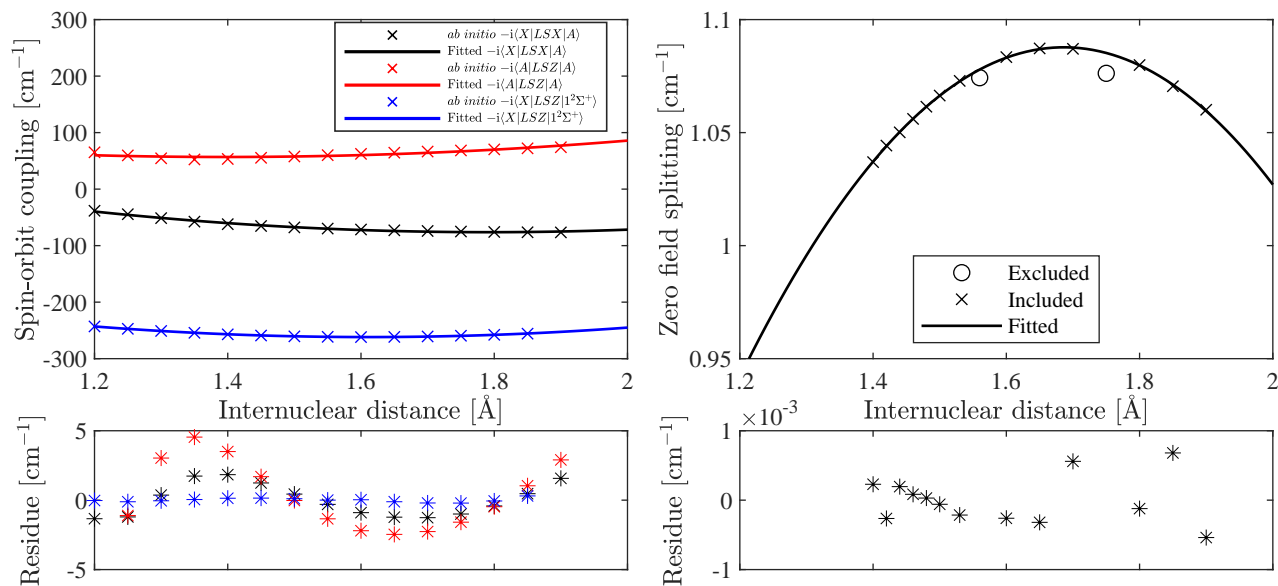The polynomial coefficients a_i are given in Table III.

FIG. 4. The calculated spin-orbit coupling curves (left) and zero field splitting curve due to spin-spin coupling (right) of VO which were fitted with polynomials. The bottom panels show the fitting residues.

9

TABLE III. Polynomial coefficients of the *ab initio* spin-orbit coupling curves.

Coefficients	$-\mathrm{i}\left\langle \mathrm{X}\,{}^4\Sigma^-\middle|\mathcal{H}_{\mathrm{LSX}}\middle|\mathrm{A}\,{}^4\Pi\right\rangle$	$-\mathrm{i}\left\langle \mathrm{A}\,{}^4\Pi\middle|\mathcal{H}_{\mathrm{LSZ}}\middle|\mathrm{A}\,{}^4\Pi\right\rangle$	$-\mathrm{i}\left\langle \mathrm{X}\,{}^4\Sigma^-\middle|\mathcal{H}_{\mathrm{LSZ}}\middle|1\,{}^2\Sigma^+\right\rangle$
a_0 [cm^{-1}]	$1.042\,001\,54 \times 10^2$	$2.116\,610\,61 \times 10^1$	$2.625\,988\,16 \times 10^1$
a_1 [cm^{-1}Å^{-1}]	$-3.735\,161\,08 \times 10^2$	$-2.217\,690\,98 \times 10^2$	$-3.574\,895\,37 \times 10^2$
a_2 [cm^{-1}Å^{-2}]	$2.585\,182\,47 \times 10^2$	$7.943\,250\,83 \times 10^1$	$1.109\,148\,62 \times 10^2$

D. Electron spin dipolar coupling

In a Cartesian representation, the zero-field splitting Hamiltonian is:[44]

$$\mathcal{H}_{\mathrm{ZFS}} = \boldsymbol{S}^{\mathsf{T}}\boldsymbol{D}\,\boldsymbol{S}. \tag{5}$$

where $\boldsymbol{S} = (S_x, S_y, S_y)$ is the spin vector operator and $\boldsymbol{D}$ is a dipolar interaction tensor. In principle axes, $\boldsymbol{D}$ is diagonal and

$$\mathcal{H}_{\mathrm{ZFS}} = D_{xx}S_x^2 + D_{yy}S_y^2 + D_{zz}S_z^2. \tag{6}$$

As a dipolar interaction tensor, $\boldsymbol{D}$ is traceless and thus $\mathcal{H}_{\mathrm{ZFS}}$ only has two degrees of freedom. In electron spin resonance spectroscopy, it is usual to define two constants, D and E, to describe zero-field splitting:

$$D = \frac{3}{2}D_{zz}, \tag{7}$$

$$E = \frac{1}{2}(D_{xx} - D_{yy}). \tag{8}$$

The Hamiltonian can be rewritten as

$$\mathcal{H}_{\mathrm{ZFS}} = D\left[S_z^2 - \frac{1}{3}\boldsymbol{S}^2\right] + E(S_x^2 - S_y^2), \tag{9}$$

with the principle axis chosen such that

$$|E| \leq \frac{1}{3}|D|.$$

For the X $^4\Sigma^-$ state of VO, $E = 0$, and hence $D_{xx} = D_{yy}$.

The calculated zero-field splitting curve is shown in the right panel of Fig. 4. The two points marked by circles were excluded from the fit. The other points were fitted with a parabolic curve whose coefficients are given in Table IV.

We used the constant experimental value[22] for the spin-rotation coupling curve, as shown in the last column of Table IV.

TABLE IV. Polynomial coefficients of the *ab initio* zero-field splitting curve $D(R)$ and the empirical spin-rotation curve $\gamma(R)$

Coefficients	$D(R)$	$\gamma(R)$
a_0 [cm^{-1}]	$-6.663\,240\,20 \times 10^{-1}$	$2.242\,111\,11 \times 10^{-2}$
a_1 [cm^{-1}Å^{-1}]	$2.080\,372\,45$	
a_2 [cm^{-1}Å^{-2}]	$-6.168\,466\,61 \times 10^{-1}$	

E. Nuclear hyperfine couplings

In a Cartesian representation, the Hamiltonian for nuclear spin – electron spin magnetic interaction is:[44]

$$\mathcal{H}_{\mathrm{HFS}} = \boldsymbol{S}^{\mathsf{T}} \boldsymbol{A} \, \boldsymbol{I}. \tag{10}$$

The hyperfine coupling tensor can be divided into an isotropic term A^{iso} and a dipolar term $\boldsymbol{A}^{\mathrm{dip}}$:

$$\mathcal{H}_{\mathrm{HFC}} = A^{\mathrm{iso}} \, \boldsymbol{S} \cdot \boldsymbol{I} + \boldsymbol{S}^{\mathsf{T}} \boldsymbol{A}^{\mathrm{dip}} \, \boldsymbol{I}. \tag{11}$$

A^{iso} is also known as the Fermi-contact interaction constant. The isotropic hyperfine coupling constant is given by

$$A^{\mathrm{iso}} = \frac{1}{3} \left(A_{xx} + A_{yy} + A_{zz} \right). \tag{12}$$

The calculated curve A^{iso} are shown in the left panel of Fig. 5. The points were fitted with a linear function, whose coefficients are given in Table V.

In the principle axis representation, the off-diagonal matrix elements of the dipolar interaction tensor $\boldsymbol{A}^{\mathrm{dip}}$ vanish. Since $\boldsymbol{A}^{\mathrm{dip}}$ is also traceless, we obtain

$$A_{xx}^{\mathrm{dip}} + A_{yy}^{\mathrm{dip}} + A_{zz}^{\mathrm{dip}} = 0. \tag{13}$$

Moreover,

$$A_{xx}^{\mathrm{dip}} = A_{yy}^{\mathrm{dip}}, \tag{14}$$

for the X$^4\Sigma^-$ state. Thus, there is only one independent parameter for $\boldsymbol{A}^{\mathrm{dip}}$. The calculated A_{zz}^{dip} term, which is plotted in the right panel of Fig. 5, was fitted with a parabolic curve whose coefficients are given in Table V.
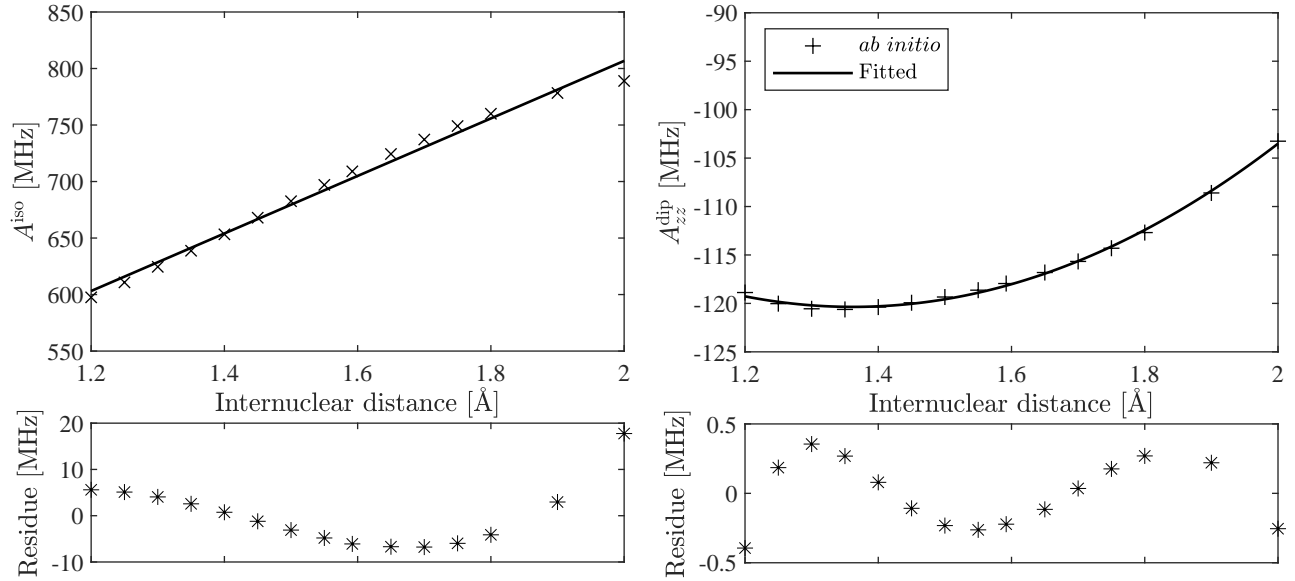
FIG. 5. The calculated A^{iso} and A_{zz}^{dip} curves of X $^4\Sigma^-$ which were fitted with polynomials. The bottom panels show the fitting residues.

TABLE V. Polynomial coefficients of the *ab initio* hyperfine coupling curves of the X $^4\Sigma^-$ state.

Coefficients	A_{zz}^{dip}	A^{iso}	eQq_0	c_I
a_0 [MHz]	$-4.353\,746\,34 \times 10^1$	$2.952\,221\,35 \times 10^2$	$-3.672\,145\,82 \times 10^3$	$3.773\,228\,18 \times 10^4$
a_1 [MHz Å^{-1}]	$-1.127\,992\,91 \times 10^2$	$2.566\,354\,89 \times 10^2$	$1.003\,490\,24 \times 10^4$	$-1.315\,887\,01 \times 10^5$
a_2 [MHz Å^{-2}]	$4.140\,638\,43 \times 10^1$		$-1.091\,669\,36 \times 10^4$	$1.825\,385\,09 \times 10^5$
a_3 [MHz Å^{-3}]			$5.915\,071\,64 \times 10^3$	$-1.262\,342\,03 \times 10^5$
a_3 [MHz Å^{-4}]			$-1.600\,684\,27 \times 10^3$	$4.351\,974\,09 \times 10^4$
a_4 [MHz Å^{-5}]			$1.733\,554\,38 \times 10^2$	$-5.995\,321\,61 \times 10^3$

The nuclear electric quadrupole coupling and nuclear spin-rotation coupling are relatively weak for the X $^4\Sigma^-$ state as shown in Fig. 6. They were fitted by polynomials, see eq. 4, whose coefficients are listed in Table V.
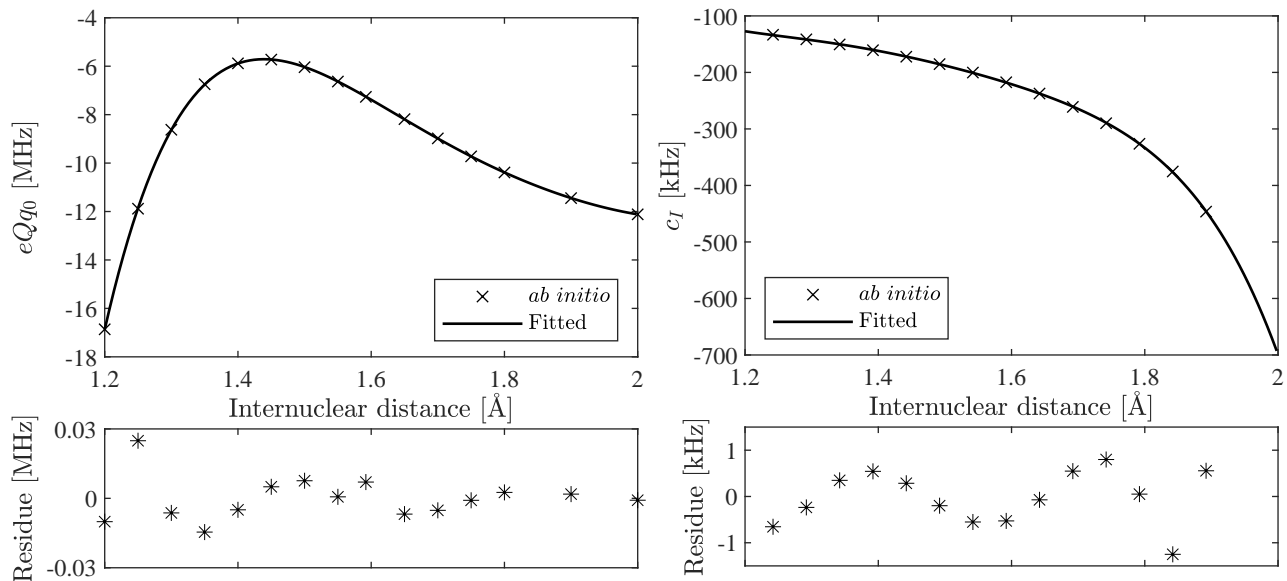
12

FIG. 6. The calculated nuclear electric quadrupole and nuclear spin-rotation coupling curve of $X\,^4\Sigma^-$ which were fitted with polynomials. The panels show the fitting residues.

IV. INFRARED SPECTRA

A. Spectroscopic model

A spectroscopic model considering the $X\,^4\Sigma^-$, $A\,^4\Pi$ and $1\,^2\Sigma^+$ states of VO was developed for the diatomic variational nuclear motion program DUO.[24] The equilibrium bond length of the $X\,^4\Sigma^-$ *ab initio* PEC was shifted by about $0.009\,\text{Å}$ so that

$$R_e = 1.5894809 \text{ Å}, \tag{15}$$

resulting in the correct rotational constant.

For the basis set in DUO we used 20 vibrationally contracted basis functions for the ground electronic states and 10 for the other two electronic states based on 401 sinc-DVR grid points, covering the internuclear distance range from 1.2 to 4 Å. The upper limit of the energy calculations was set to $50\,000\,\text{cm}^{-1}$, which is just below the first dissociation limit of VO; the energy levels of interest for this work are expected to be below $10\,000\,\text{cm}^{-1}$ which is close to the T_e value of $A\,^4\Pi$ and is also below the discontinuity point in the PEC of the $X\,^4\Sigma^-$ state. This range covers vibrational levels up to $v = 10$. Thus, the 20 vibrational contracted basis functions are enough to give converged energy levels.

The coupling constants used in DUO follow the definitions generally adopted in experimental studies.[25] Some constants have the same definition as those given by quantum chemistry programs. For example, the Fermi-contact coupling constant is just A^{iso}

$$b_{\text{F}} = A^{\text{iso}}. \tag{16}$$

Definitions of others are different and we give the relevant interconversion formulae below.

In a Cartesian representation, the Hamiltonian of a diagonal electron spin-spin dipolar interaction of diatomic molecule is

$$\mathcal{H}_{\text{SS}} = \frac{2}{3}\lambda \left(3S_z^2 - \boldsymbol{S}^2\right), \tag{17}$$

where $\boldsymbol{S}$ is the electron spin angular momentum and S_z is its z component. Comparing $\mathcal{H}_{\text{SS}}$ with $\mathcal{H}_{\text{ZFS}}$, we have

$$\lambda = \frac{1}{2}D. \tag{18}$$

In a Cartesian representation, the Hamiltonian of the nuclear spin-electron spin dipolar interaction is given by

$$\begin{aligned}
\mathcal{H}_{\text{dip}} = {} & \frac{1}{3}c\left(3I_z S_z - \boldsymbol{I} \cdot \boldsymbol{S}\right) \\
& + \frac{1}{2}d\left[S_+ I_+ \exp(-2\mathrm{i}\phi) + S_- I_- \exp(2\mathrm{i}\phi)\right] \\
& e\Bigg[\left(S_- I_z + S_z I_-\right)\exp(\mathrm{i}\phi) \\
& + \left(S_+ I_z + S_z I_+\right)\exp(-\mathrm{i}\phi)\Bigg],
\end{aligned} \tag{19}$$

where c, d and e are three nuclear spin-electron spin dipolar interaction constants; $\boldsymbol{I}$ is the nuclear spin angular momentum; I_z, I_+ and I_- are the components of $\boldsymbol{I}$; S_z, S_+ and S_- are the components of $\boldsymbol{S}$; ϕ is the variable of spherical harmonics, see Eq. 4 of Slotterback *et al.*[45]. Comparing the Hamiltonian with the matrix elements of $\boldsymbol{I}^{\mathsf{T}} \boldsymbol{A}^{\text{dip}} \boldsymbol{S}$, we have:

$$A_{xx}^{\text{dip}} = -\frac{c}{3} + d\cos(2\phi), \tag{20}$$

$$A_{yy}^{\text{dip}} = -\frac{c}{3} - d\cos(2\phi), \tag{21}$$

$$A_{zz}^{\text{dip}} = \frac{2c}{3}. \tag{22}$$

For the ground state, we have $A_{xx}^{\text{dip}} = A_{yy}^{\text{dip}}$. The only non-vanishing constant is

$$c = \frac{3}{2}A_{zz}. \tag{23}$$

TABLE VI. The empirical hyperfine coupling constants for $v = 0$ given in Table 4 of Flory and Ziurys[22] and the calculated diagonal hyperfine matrix elements $\langle v = 0|\cdot|v = 0\rangle$ of X $^4\Sigma^-$. All values are given in MHz.

Parameter	b_F	c	c_I	eQq_0
Empirical[22]	778.737(66)	-129.84(19)	0.1928(51)	-2.5(1.3)
Ab initio	703.2540	-177.1301	-0.2191	-7.2987

Dipole moments were also obtained from our *ab initio* calculations. However, they are not as accurate as the dipole moments calculated by McKemmish *et al.*[35] using the finite-field method. Thus, we used the permanent dipole moment of X $^4\Sigma^-$ in Ref.[35] to compute Einstein-A coefficients and hence transition intensities.

B. Hyperfine matrix elements in the representation of the vibrational basis set

We use a fully variational method to calculated the hyperfine structure of the VO X $^4\Sigma^-$ state. The final wavefunctions have non-zero projections on all contracted vibrational basis functions. See our previous paper[25] for more details. The absolute values of the Fermi-contact matrix elements $\langle v|b_\mathrm{F}(R)|v'\rangle$ are plotted in Fig. 7. The values decrease dramatically with the difference between v' and v, *i.e.*, the diagonal matrix element $\langle v|b_\mathrm{F}(R)|v\rangle$ dominates the Fermi-contact interaction in the vibrational states. The reason for the phenomenon is that the lowest 11 vibrational levels of X $^4\Sigma^-$ do not interact with other vibronic levels in our model. Thus, the diagonal Fermi-contact matrix elements in the VO X $^4\Sigma^-$ state provided should be equivalent to the spectroscopic coupling constants used in effective Hamiltonian methods. We list all the diagonal hyperfine matrix elements of the lowest 11 vibrational levels of X $^4\Sigma^-$ in Table VI. Compared to the measured constants of the $v = 0$ level[22], the absolute values of the calculated Fermi-contact matrix elements are smaller while the nuclear spin-electron spin dipolar matrix elements are larger. For VO, the nuclear spin-rotation and nuclear electric quadrupole interactions are much weaker than the other hyperfine interactions. The corresponding matrix elements are of similar magnitude to the experimental values.
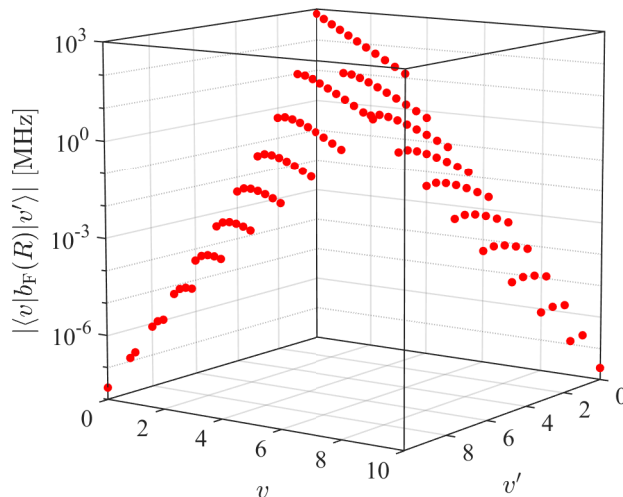
15

FIG. 7. Absolute values of Fermi-contact matrix elements $\langle v|b_F(R)|v'\rangle$ of $X\,^4\Sigma^-$ for $v \leq 10$ and $v' \leq 10$.

C. Hyperfine eigenstates and transitions

A hyperfine-resolved line list was generated based on the spectroscopic model. DUO provides data in ExoMol format[46] which means energies with quantum numbers are in a `.states` file and the Einstein-A coefficients for each transitions are in a `.trans` file. Examples of calculated energies and transitions extracted from the output files are given as supplementary materials. In DUO's outputs, the eigenstates are printed in the increasing order of the final angular momentum, which is F here. All energies are given relative to the non-hyperfine zero-point energy *i.e.*, which corresponds to $J = 0.5, +, v = 0$.

A hyperfine-resolved set of empirical energies of VO has recently been obtained[17] using the MARVEL (measured active vibration-rotation energy levels) procedure, which includes 6603 validated transitions from three experimental sources[22,40,47] and gives 1256 hyperfine-resolved energy terms for the $v = 0$ state of $X\,^4\Sigma^-$. We compare our calculated energies with all the MARVEL ones, as illustrated in the left panel of Fig. 8. The energy differences indicate that the *ab initio* fine and hyperfine coupling curves require further refinement to give accurate electron and nuclear spin splitting.

In order to illustrate the potential of such refinement on the quality of the energy cal-culations, we shifted some fine and hyperfine coupling curves in our model such that the

corresponding diagonal matrix elements $\langle v = 0|\cdot|v = 0\rangle$ have the same values as the experimental spectroscopic constants determined by Flory and Ziurys [22]. The shifted parameters are listed in Table VII. The right panel of Fig. 8 demonstrates the differences between the calculated and MARVEL energies in this case. The calculation accuracy improves significantly with use of the shifted curves.

TABLE VII. Final a_0 values for four shifted curves: spin-orbit interaction of $X\,^4\Sigma^-$-$1\,^2\Sigma^+$; $\gamma(R)$, $A^{\mathrm{iso}}(R)$ and $A_{zz}^{\mathrm{dip}}(R)$ of $X\,^4\Sigma^-$.

Curve	State(s)	a_0 value [cm^{-1}]
Spin-orbit	$X\,^4\Sigma^- - 1\,^2\Sigma^+$	$5.968\,341\,65 \times 10^1$
$\gamma(R)$	$X\,^4\Sigma^-$	$2.218\,113\,85 \times 10^{-2}$
$A^{\mathrm{iso}}(R)$	$X\,^4\Sigma^-$	$1.270\,963\,58 \times 10^{-2}$
$A_{zz}^{\mathrm{dip}}(R)$	$X\,^4\Sigma^-$	$-4.006\,617\,87 \times 10^{-4}$

There are four states (shown as red circles in the lefthand panel) whose calculation errors are greater than $0.1\,\mathrm{cm}^{-1}$, so outside the range of the righthand panel of Fig. 8. The energy levels between 100 to 200 cm^{-1} have larger uncertainties than the others, as shown in the right panel. As discussed previously,[22,40,47] this behavior arises from the internal perturbations near $N = 15$, resulting in an avoided crossing structure as shown the lefthand panel of Fig. 9. The righthand panel of Fig. 9 illustrates the interactions of states in the F_2 series of $X\,^4\Sigma^-$. The interactions mix energy levels which makes it difficult to assign quantum number to these states. The globally J-dependent systematic error can be attributed to inaccurate spin-orbit, spin-spin and spin-rotation coupling curves. We plan to refine these curves in our future work.

D. Transition intensities and lifetime

The hyperfine resolved VO line list was used to generate spectra of the $X\,^4\Sigma^-$ band using the program EXOCROSS.[48] The left panel of Fig. 10 compares cross sections calculated in this work at $T = 2200$ K. We used a Gaussian lineshape function for each isolated line and the linewidth was chosen as $0.2\,\mathrm{cm}^{-1}$. The linewidth is wider than hyperfine splittings and thus, the cross section profiles are blended. As a result, the hyperfine resolved and unresolved
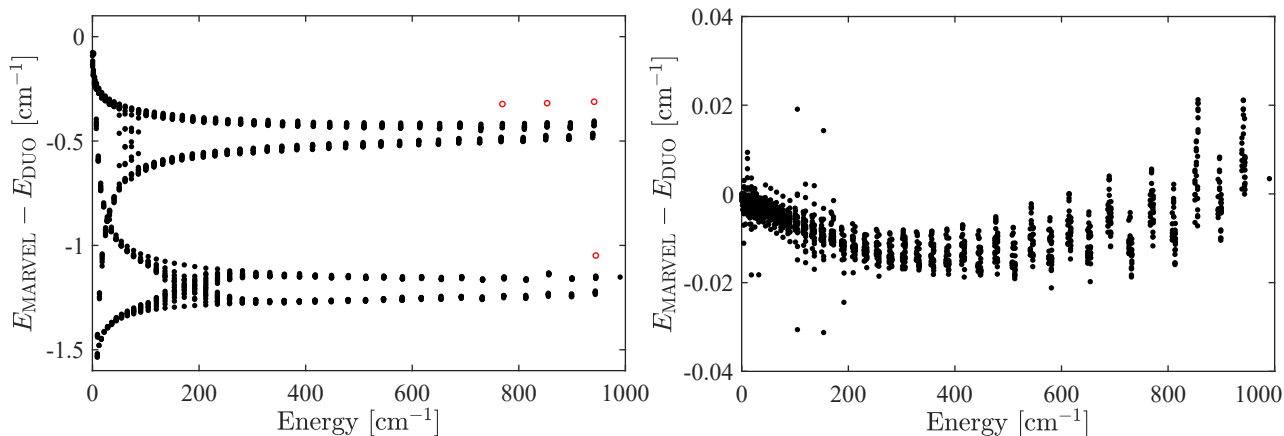
FIG. 8. Energy differences between results of DUO and MARVEL analysis when using *ab initio* curves. Left: only the R_e value of $X\,^4\Sigma^-$ was shifted to give correct rotational constants. Right: several other curves were also shifted to reproduce the coupling constants given in Table 4 of Flory and Ziurys [22].
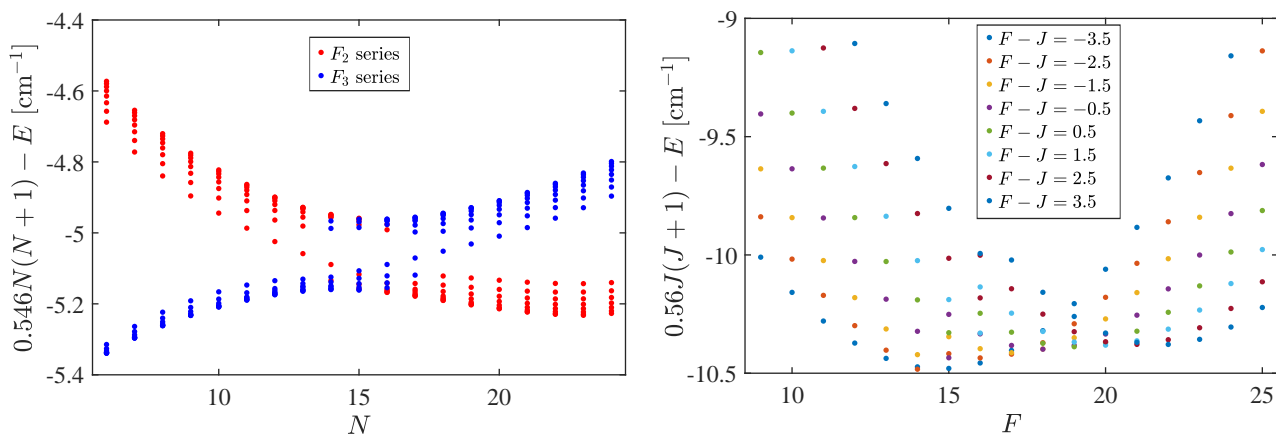

FIG. 9. The lefthand panel shows the avoided crossing structure of the F_2 and F_3 levels of $X\,^4\Sigma^-$. The righthand panel shows the mixing energy levels in the F_2 series of $X\,^4\Sigma^-$. Note that, DUO does not use the quantum number N. N is given here simply for the clarity of the figure and was obtained using the rule $N = J - 0.5$ for the F_2 series and $N = J + 0.5$ for the F_3 series.

cross sections agree well with each other. Note that, in this work, we only calculated the transitions within the ground state of VO without considering the A-X transition dipole moment contribution to line strengths. In practice, A-X spin-orbit coupling mixes the wavefunctions of the two electronic states meaning spectra are increasingly determined by

18

both the X-X and the A-X electric dipole moment curves; transitions above $6000\,\text{cm}^{-1}$ are much stronger when the A-X transition dipole moment is included. We do not attempt to properly model the A state here so we leave the discussion of the interaction of this and other electronic states to future work.

Only hyperfine transitions with narrow broadening parameters are distinguishable in high-resolution experiments, see *e.g.* the work of Flory and Ziurys[22]. We simulated the spectra of the eight hyperfine transitions near $9.73\,\text{cm}^{-1}$ with different line widths. As shown in the top-right panel of Fig. 10, the hyperfine transitions are completely blended when the half width at half maximum is $0.002\,\text{cm}^{-1}$. However, due to the uneven line strength distribution of hyperfine transitions, the shape and center of the blended profile differs from the one simulated from the line list without considering the nuclear hyperfine couplings, which is shown in the bottom-right panel of Fig. 10. Similar conclusions were drawn from the VO MARVEL study[17] where attempts to deperturb the hyperfine-resolved energies by setting the hyperfine constants to zero were found to give poor results.
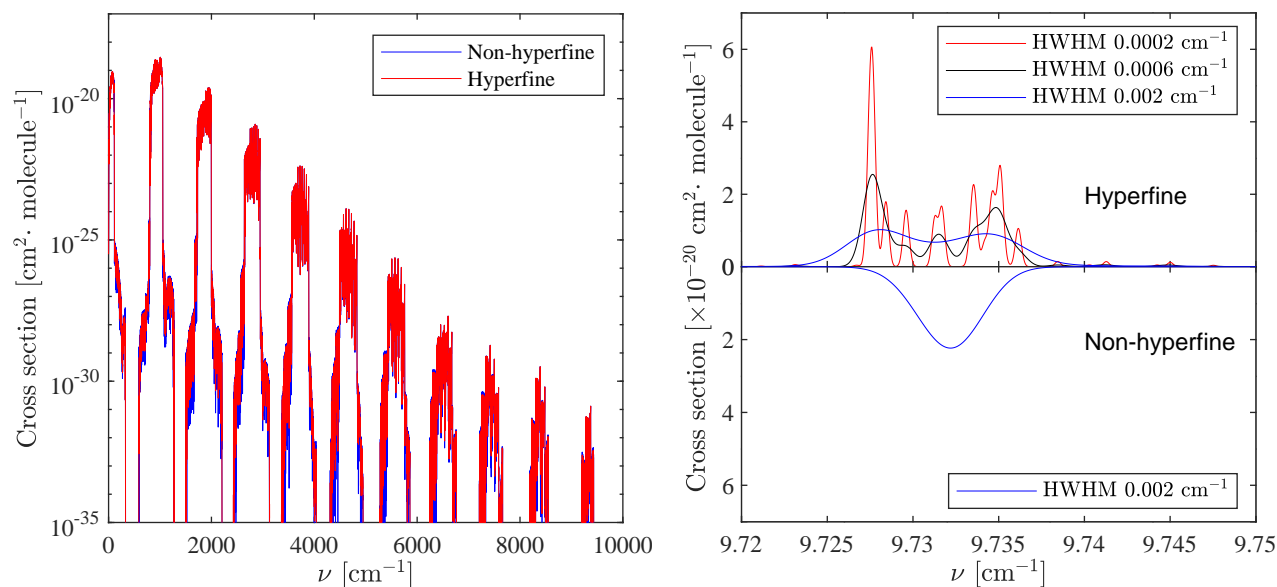

FIG. 10. Comparison of VO IR cross sections at 2200 K. Left: the cross sections were calculated with Gaussian profiles whose linewidth are $0.2\,\text{cm}^{-1}$. Right: the cross sections were calculated with Gaussian profiles of different line widths in a narrow range. 'Non-hyperfine' in this and following figures is a short notation which means that the spectra were simulated without considering nuclear hyperfine couplings.

Figure 11 illustrates the hyperfine splitting of non-hyperfine transitions near $9.77\,\mathrm{cm}^{-1}$. Due to the nuclear spin, both the upper and lower non-hyperfine energy levels split to several hyperfine levels and the combinations of them give a lot hyperfine transitions as shown in the top panel. In the middle panel, we plot the two strongest non-hyperfine transition in this region. The intensity of each non-hyperfine transition is approximately the sum of intensities of the eight strong hyperfine transitions nearby but not rigorously equal to it. These strong hyperfine transitions were observed by Flory and Ziurys[22]. Our calculated positions agree well with the measured values. Note that, the hyperfine transitions are not necessarily distributed around the non-hyperfine transitions, as the transitions near $9.8\,\mathrm{cm}^{-1}$ indicate. We emphasize again that in this paper the word 'non-hyperfine' is used as shorthand notation for the terms given without considering nuclear hyperfine interactions. The word has a different meaning from 'hyperfine unresolved' which is used to describe blended hyperfine transitions.

As the nuclear spin of $^{51}\mathrm{V}^{16}\mathrm{O}$ is 7/2, theoretically, one can get 'forbidden' dipole transitions up to $|\Delta J| = 8$. Table VIII lists eight transitions corresponding to $|\Delta J| = 1, 2, \cdots 8$. As J is no longer a good quantum number for hyperfine structure, the J' and J'' values here are the values of dominant basis functions. The higher $|\Delta J|$ transitions are much weaker while transitions with $|\Delta J| = 2$ or 3 have has Einstein-A of similar magnitude to the 'allowed' $|\Delta J| = 1$ one. We are not aware of the observation of such forbidden lines within the $\mathrm{X}\,^4\Sigma^-$ state. However, $|\Delta J| = 2$ (O and S branches) driven by hyperfine couplings have been observed in both hyperfine-resolved[40,47] and unresolved[23,49] rovibronic spectra.

The lifetimes of hyperfine and non-hyperfine eigenstates of the lowest vibrational level of $\mathrm{X}\,^4\Sigma^-$ were calculated by using EXOCROSS, and compared in Fig. 12. The hyperfine states have similar lifetimes as the corresponding non-hyperfine state.

V. CONCLUSION

In this work, we investigate the hyperfine-resolved infra-red spectra of VO $\mathrm{X}\,^4\Sigma^-$ electronic state. The fine and hyperfine coupling curves required to construct the spectroscopic model were calculated *ab initio* where possible but then scaled to reproduce the observed hyperfine structure. The hyperfine splitting of $\mathrm{X}\,^4\Sigma^-$ is mainly determined by the Fermi-contact and electron spin-nuclear spin dipolar interactions. Nevertheless, we also included

20

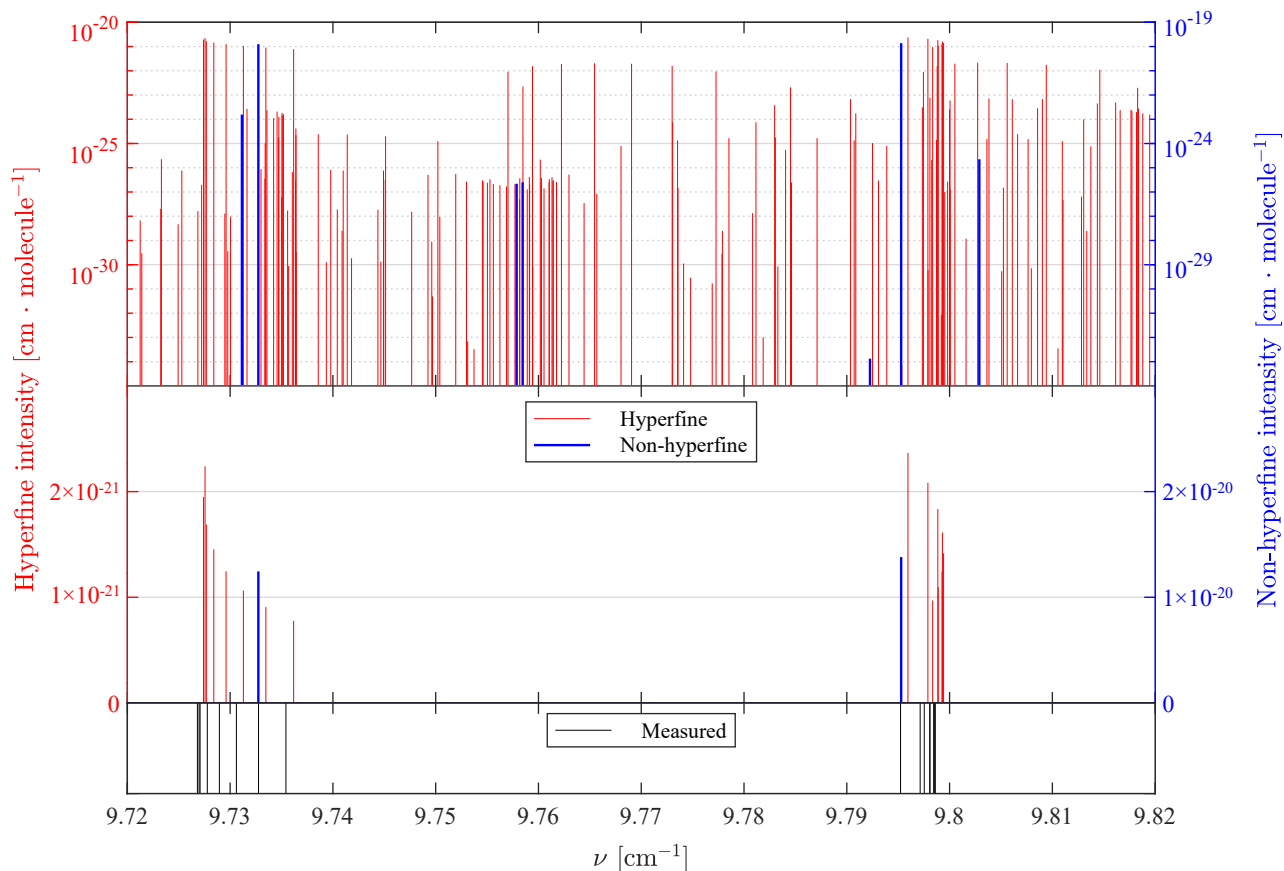FIG. 11.   Comparison of the calculated (top and middle) and measured (bottom) transitions near $9.77\,\mathrm{cm}^{-1}$. The line intensities in the top and middle panels were calculated at $208\,\mathrm{K}$. The middle panel only demonstrates the strong transitions. The hyperfine resolved line positions in the bottom panel were measured by Flory and Ziurys [22].

the nuclear spin-rotation and nuclear electric quadrupole coupling curves in our calculation. The hyperfine resolved and unresolved cross sections show good consistency with each other when using wide line broadening parameters. The comparison between calculated and and empirical energy levels reveals the inaccuracy of our *ab initio* fine and hyperfine coupling curves even when computed using state-of-the-art methods and hence the need for empirical refinement. We plan to refine these curves and use them to generate a full, hyperfine-resolved line list for VO in future work.

TABLE VIII. Transitions corresponding to $|\Delta J| = 1 \ldots 8$.

| $|\Delta J|$	ν [cm^{-1}]	A [s^{-1}]	E' [cm^{-1}]	F'	parity$'$	J'	v'	Ω'	E'' [cm^{-1}]	F''	parity$''$	J''	v''	Ω''
1	890.2463	6.7981E+01	9370.8835	0	-	3.5	10	0.5	8480.6371	1	+	4.5	9	0.5
2	880.4238	5.6402E+01	8635.9538	14	+	16.5	9	1.5	7755.5299	15	-	18.5	8	1.5
3	921.1696	2.3566E+01	9975.2714	37	-	35.5	10	0.5	9054.1018	36	+	32.5	9	1.5
4	942.0396	2.1003E-01	3909.3168	9	-	6.5	4	0.5	2967.2771	10	+	10.5	3	0.5
5	925.0690	6.9014E-06	9437.0199	11	+	11.5	10	1.5	8511.9509	10	-	6.5	9	0.5
6	923.5723	1.6667E-09	9435.5233	11	+	12.5	10	0.5	8511.9509	10	-	6.5	9	0.5
7	950.5501	1.8763E-15	9462.5010	11	+	13.5	10	1.5	8511.9509	10	-	6.5	9	0.5
8	949.0735	1.6573E-18	9461.0244	11	+	14.5	10	0.5	8511.9509	10	-	6.5	9	0.5
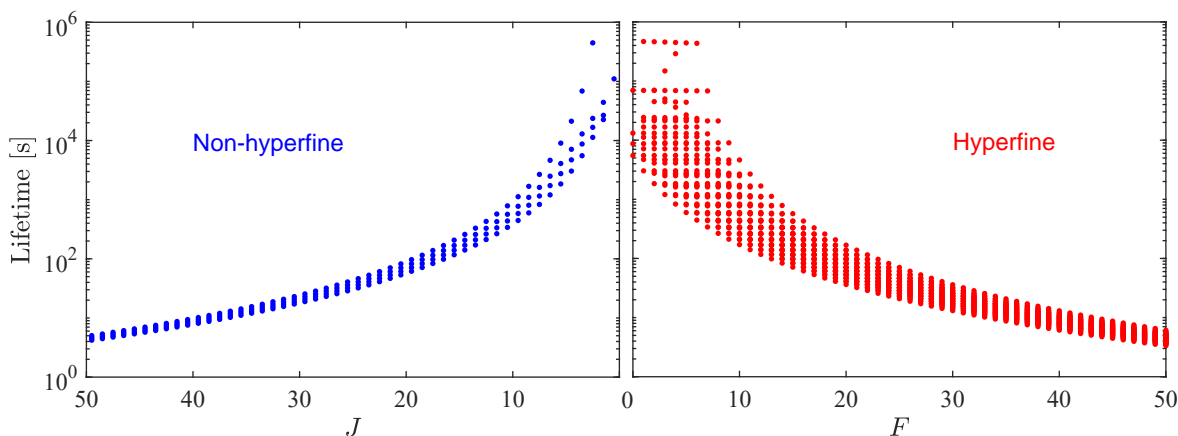
FIG. 12. Comparison of lifetimes corresponding to the lower rotational levels of X $^4\Sigma^-$, $v = 0$. The $J = 0.5$ levels which have much longer lifetimes were not plotted in this figure.

SUPPLEMENTARY MATERIAL

The Duo input file used in this work is given as supplementary material; our potential energy curves are included as part of this input file. Two tables, which lists the sample states and transitions calculated from the input, are given as supplementary materials.

ACKNOWLEDGMENTS

DATA AVAILABILITY

The open access programs ExoCross and Duo are available from github.com/exomol.

REFERENCES

[1] P. F. Bernath, Int. Rev. Phys. Chem. **28**, 681 (2009).

[2] N. Madhusudhan and S. Seager, Astrophys. J. **725**, 261 (2010).

[3] T. M. Evans, D. K. Sing, H. R. Wakeford, N. Nikolov, G. E. Ballester, B. Drummond, T. Kataria, N. P. Gibson, D. S. Amundsen, and J. Spake, Astrophys. J. **822**, L4 (2016).

[4] J. D. Turner, R. M. Leiter, L. I. Biddle, K. A. Pearson, K. K. Hardegree-Ullman, R. M. Thompson, J. K. Teske, I. T. Cates, K. L. Cook, M. P. Berube, M. N. Nieberding, C. K. Jones, B. Raphael, S. Wallace, Z. T. Watson, and R. E. Johnson, Mon. Not. Roy. Astron. Soc. **472**, 3871 (2017).

[5] E. Palle, G. Chen, J. Prieto-Arranz, G. Nowak, F. Murgas, L. Nortmann, D. Pollacco, K. Lam, P. Montanes-Rodriguez, H. Parviainen, and N. Casasayas-Barris, Astron. Astrophys. **602** (2017), 10.1051/0004-6361/201731018.

[6] A. Tsiaras, I. P. Waldmann, T. Zingales, M. Rocchetto, G. Morello, M. Damiano, K. Karpouzas, G. Tinetti, L. K. McKemmish, J. Tennyson, and S. N. Yurchenko, Astron. J. **155**, 156 (2018).

[7] J. M. Goyal, N. Mayne, B. Drummond, D. K. Sing, E. Hebrard, N. Lewis, P. Tremblin, M. W. Phillips, T. Mikal-Evans, and H. R. Wakeford, Mon. Not. Roy. Astron. Soc. **498**, 4680 (2020).

[8] N. K. Lewis, H. R. Wakeford, R. J. MacDonald, J. M. Goyal, D. K. Sing, J. Barstow, D. Powell, T. Kataria, I. Mishra, M. S. Marley, N. E. Batalha, J. I. Moses, P. Gao, T. J. Wilson, K. L. Chubb, T. Mikal-Evans, N. Nikolov, N. Pirzkal, J. J. Spake, K. B. Stevenson, J. Valenti, and X. Zhang, Astrophys. J. Lett. **902**, L19 (2020).

[9] L. K. McKemmish, T. Masseron, S. Sheppard, E. Sandeman, Z. Schofield, T. Furtenbacher, A. G. Császár, J. Tennyson, and C. Sousa-Silva, Astrophys. J. Suppl. Ser. **228**, 15 (2017).

[10] S. K. Nugroho, H. Kawahara, K. Masuda, T. Hirano, T. Kotani, and A. Tajitsu, Astrophys. J. **154**, 221 (2017).

[11] D. B. Serindag, I. A. G. Snellen, and P. Molliere, Astron. Astrophys. **655**, A69 (2021).

[12] B. Prinoth, H. J. Hoeijmakers, D. Kitzmann, E. Sandvik, J. Seidel, V, M. Lendl, N. W. Borsato, B. Thorsbro, D. R. Anderson, D. Barrado, K. Kravchenko, R. Allart, V. Bourrier, H. M. Cegla, D. Ehrenreich, C. Fisher, C. Lovis, A. Guzman-Mesa, S. Grimm, M. Hooton, B. M. Morris, M. Oreshenko, L. Pino, and K. Heng, Nature Astr. **6**, 449 (2022).

[13] L. K. McKemmish, S. N. Yurchenko, and J. Tennyson, Mon. Not. Roy. Astron. Soc. **463**, 771 (2016).

[14] S. de Regt, A. Y. Kesseli, I. A. G. Snellen, S. R. Merritt, and K. L. Chubb, Astron. Astrophys. **661**, A109 (2022).

[15] J. Tennyson, S. N. Yurchenko, A. F. Al-Refaie, V. H. J. Clark, K. L. Chubb, E. K. Conway, A. Dewan, M. N. Gorman, C. Hill, A. E. Lynas-Gray, T. Mellor, L. K. McKemmish, A. Owens, O. L. Polyansky, M. Semenov, W. Somogyi, G. Tinetti, A. Upadhyay, I. Waldmann, Y. Wang, S. Wright, and O. P. Yurchenko, J. Quant. Spectrosc. Radiat. Transf. **255**, 107228 (2020).

[16] A. J. Merer, Annu. Rev. Phys. Chem. **40**, 407 (1989).

[17] C. A. Bowesman, H. Akbari, S. Hopkins, S. N. Yurchenko, and J. Tennyson, J. Quant. Spectrosc. Radiat. Transf. (2022), 10.1016/j.jqsrt.2022.108295.

[18] W. H. Hocking, A. J. Merer, and D. J. Milton, Can. J. Phys. **59**, 266 (1981).

[19] A. S.-C. Cheung, R. C. Hansen, and A. J. Merer, J. Mol. Spectrosc. **91**, 165 (1982).

[20] R. D. Suenram, G. T. Fraser, F. J. Lovas, and C. W. Gillies, J. Mol. Spectrosc. **148**, 114 (1991).

[21] A. G. Adam, M. Barnes, B. Berno, R. D. Bower, and A. J. Merer, J. Mol. Spectrosc. **170**, 94 (1995).

[22] M. A. Flory and L. M. Ziurys, J. Mol. Spectrosc. **247**, 76 (2008).

[23] A. S. C. Cheung, P. G. Hajigeorgiou, G. Huang, S. Z. Huang, and A. J. Merer, J. Mol. Spectrosc. **163**, 443 (1994).

[24] S. N. Yurchenko, L. Lodi, J. Tennyson, and A. V. Stolyarov, Comput. Phys. Commun. **202**, 262 (2016).

[25] Q. Qu, S. N. Yurchenko, and J. Tennyson, J. Chem. Theory Comput. **18**, 1808 (2022).

[26] C. W. Bauschlicher and P. Maitre, Theor. Chim. Acta. **90**, 189 (1995).

[27] A. J. Bridgeman and J. Rothery, J. Chem. Soc. Dalton , 211 (2000).

[28] M. Calatayud, B. Silvi, J. Andres, and A. Beltran, Chem. Phys. Lett. **333**, 493 (2001).

[29] E. Broclawik and T. Borowski, Chem. Phys. Lett. **339**, 433 (2001).

[30] B. Dai, K. M. Deng, J. L. Yang, and Q. S. Zhu, J. Chem. Phys. **118**, 9608 (2003).

[31] M. Pykavy and C. van Wullen, J. Phys. Chem. A **107**, 5566 (2003).

[32] H. J. Kulik and N. Marzari, J. Chem. Phys. **133**, 114103 (2010).

[33] E. Miliordos and A. Mavridis, J. Phys. Chem. A **111**, 1953 (2007).

[34] O. Hübner, J. Hornung, and H.-J. Himmel, J. Chem. Phys. **143**, 024309 (2015).

[35] L. K. McKemmish, S. N. Yurchenko, and J. Tennyson, Mol. Phys. **114**, 3232 (2016).

[36] T. Jiang, Y. Chen, N. A. Bogdanov, E. Wang, A. Alavi, and J. Chen, J. Chem. Phys. , 164302 (2021).

[37] H. J. Werner, P. J. Knowles, G. Knizia, F. R. Manby, M. Schütz, P. Celani, W. Györffy, D. Kats, T. Korona, R. Lindh, A. Mitrushenkov, G. Rauhut, K. R. Shamasundar, T. B. Adler, R. D. Amos, A. Bernhardsson, A. Berning, D. L. Cooper, M. J. O. Deegan, A. J. Dobbyn, F. Eckert, E. Goll, C. Hampel, A. Hesselmann, G. Hetzer, T. Hrenar, G. Jansen, C. Köppl, Y. Liu, A. W. Lloyd, R. A. Mata, A. J. May, S. J. McNicholas, W. Meyer, M. E. Mura, A. Nicklass, D. P. O'Neill, P. Palmieri, D. Peng, K. Pflüger, R. Pitzer, M. Reiher, T. Shiozaki, H. Stoll, A. J. Stone, R. Tarroni, T. Thorsteinsson, and M. Wang, "Molpro, version 2015.1, a package of ab initio programs," http://www.molpro.net (2015).

[38] T. H. Dunning, J. Chem. Phys. **90**, 1007 (1989).

[39] N. B. Balabanov and K. A. Peterson, J. Chem. Phys. **123**, 064107 (2005).

[40] A. G. Adam, M. Barnes, B. Berno, R. D. Bower, and A. J. Merer, J. Mol. Spectrosc. **170**, 94 (1995).

[41] W. S. Hopkins, S. M. Hamilton, and S. R. Mackenzie, J. Chem. Phys. **130**, 144308 (2009).

[42] F. Neese, Wiley Interdiscip. Rev.-Comput. Mol. Sci. **2**, 73 (2012).

[43]K. Aidas, C. Angeli, K. L. Bak, V. Bakken, R. Bast, L. Boman, O. Christiansen, R. Cimiraglia, S. Coriani, P. Dahle, E. K. Dalskov, U. Ekström, T. Enevoldsen, J. J. Eriksen, P. Ettenhuber, B. Fernández, L. Ferrighi, H. Fliegl, L. Frediani, K. Hald, A. Halkier, C. Hättig, H. Heiberg, T. Helgaker, A. C. Hennum, H. Hettema, E. Hjertenaes, S. Høst, I.-M. Høyvik, M. F. Iozzi, B. Jansík, H. J. A. Jensen, D. Jonsson, P. Jørgensen, J. Kauczor, S. Kirpekar, T. Kjaergaard, W. Klopper, S. Knecht, R. Kobayashi, H. Koch, J. Kongsted, A. Krapp, K. Kristensen, A. Ligabue, O. B. Lutnaes, J. I. Melo, K. V. Mikkelsen, R. H. Myhre, C. Neiss, C. B. Nielsen, P. Norman, J. Olsen, J. M. H. Olsen, A. Osted, M. J. Packer, F. Pawlowski, T. B. Pedersen, P. F. Provasi, S. Reine, Z. Rinkevicius, T. A. Ruden, K. Ruud, V. V. Rybkin, P. Sałek, C. C. M. Samson, A. S. de Merás, T. Saue, S. P. A. Sauer, B. Schimmelpfennig, K. Sneskov, A. H. Steindal, K. O. Sylvester-Hvid, P. R. Taylor, A. M. Teale, E. I. Tellgren, D. P. Tew, A. J. Thorvaldsen, L. Thøgersen, O. Vahtras, M. A. Watson, D. J. D. Wilson, M. Ziolkowski, and H. Ågren, Wiley Interdiscip. Rev.-Comput. Mol. Sci. **4**, 269 (2014).

[44]A. Schweiger and G. Jeschke, *Principles of pulse electron paramagnetic resonance* (Oxford University Press, 2001).

[45]T. J. Slotterback, S. G. Clement, K. C. Janda, and C. M. Western, J. Chem. Phys. **103**, 9125 (1995).

[46]J. Tennyson, C. Hill, and S. N. Yurchenko, in *6th international conference on atomic and molecular data and their applications ICAMDATA-2012*, AIP Conference Proceedings, Vol. 1545 (AIP, New York, 2013) pp. 186–195.

[47]A. S. C. Cheung, R. C. Hansen, and A. J. Merer, J. Mol. Spectrosc. **91**, 165 (1982).

[48]S. N. Yurchenko, A. F. Al-Refaie, and J. Tennyson, Astron. Astrophys. **614**, A131 (2018).

[49]L. Karlsson, B. Lindgren, C. Lundevall, and U. Sassenberg, J. Mol. Spectrosc. **181**, 274 (1997).